

The transition to continuous unloading: Differentiating storms and substorms in magnetospheric dynamics

James P. Smith and Wendell Horton

Institute for Fusion Studies, University of Texas at Austin

D. N. Baker

Laboratory for Atmos. and Space Physics, University of Colorado, Boulder

13 May 1999

Abstract

We present a new paradigm for the driving of storms and substorms. Using a model that tracks the major energy components of the magnetosphere-ionosphere system, we demonstrate that both storms and substorms can be obtained from the same dynamical system for different levels of forcing. To say that storms are made up of substorms would be incorrect. Instead we see that periodic substorms result for weak forcing, while a steady storm ensues for strong forcing, with a continuous transition between the two. There is thus an inverse bifurcation in the state of the system with respect to driving between substorms and storms. While the forcing may initially be weak and produce substorms preceding a storm, they are, in fact, topologically different states of the magnetosphere (an attractor of dimension one for substorms and an attractor of dimension zero for storms). The properties of both states are discussed in detail. We are also able to characterize two types of unloading of tail flux: storage-unloading and continuous unloading. The rapid storage-unloading process is shown to be equivalent to the substorm expansion onset. The hypothesis is advanced that the state of continuous unloading represents a magnetic storm.

1 Introduction

While substorms were originally conceived by Chapman as the building blocks of storms, with storms being simply a superposition of substorms, several recent studies of the relationship between the two have contravened this hypothesis [McPherron, 1997; Rostoker et al., 1997]. Yet it hardly seems likely that both events could have the same forcing (the solar wind) and use the same dynamical system (the magnetosphere) and be completely unrelated.

Extensive studies of magnetospheric response to solar wind forcing [McPherron et al., 1988; Bargatze et al., 1985; Klimas et al., 1991] have concluded that the response of the magnetosphere depends strongly on the state of the magnetosphere at the beginning of forcing, as well as the solar wind forcing itself. Local linear prediction filter studies [Klimas

et al., 1997] provide the most compelling evidence, showing a near perfect predictive ability if the coefficients of the filter are chosen based on the present state of the magnetosphere and its recent history. It is therefore reasonable to expect any model of the magnetosphere to exhibit a dependence on the previous history of the system.

The WINDMI model used in this study is a low dimensional nonlinear global model which characterizes the major energy components of the magnetosphere as: the lobe magnetic energy $\int_{lobe} \frac{B^2}{2\mu_0} d^3x \approx \frac{1}{2}LI^2$, the magnetic energy of the nightside region-1 currents, $\int_1 \frac{B^2}{2\mu_0} d^3x \approx \frac{1}{2}L_i I_i^2$, and the interaction energy of the two current systems, $-MII_i$; the perpendicular mass flow kinetic energy in the plasma sheet and the ionosphere region-1 currents, $\int_{PS+ion.} \frac{1}{2}\rho u_{\perp}^2 d^3x \approx \frac{1}{2}CV^2 + \frac{1}{2}C_i V_i^2$, the parallel mass flow kinetic energy of the plasma sheet, $\int_{PS} \frac{1}{2}\rho u_{\parallel}^2 d^3x \approx K_{\parallel}$, and the thermal energy of the plasma sheet, $\int_{PS} \frac{3}{2}P d^3x \approx \frac{3}{2}\Omega P$. The state space, $\mathbf{X}(t)$, of the low-dimensional two-cell description derived by Horton and Doxas [1998] is given by $\mathbf{X}(t) = \{I, V, P, K_{\parallel}, I_i, V_i\}$. (This is “two-cell” in the dynamical systems sense, where we have two interacting physical regions, and does not refer to the DP-2 current system.) Each of these six state variables can be seen (from the above definitions) to characterize one of the major energy components of the coupled magnetosphere-ionosphere system. Their evolution is given by six ordinary differential equations which are driven only by the eastward component of the convection electric field ($V_x B_z$) applied to the magnetopause by the solar wind. A graphical, but complete, description of the model equations is given in Figure 1. Since all of the terms of the model are included in this figure, the equations can be reconstructed in a straightforward manner. For example, looking at the parallel flow energy, we can see that the equation is $\dot{K}_{\parallel} = P^{1/2}V - K_{\parallel}$.

Fig. 1

The derivation of this model is described in detail elsewhere [Horton and Doxas 1996, 1998]. The Euler-Lagrange equations from the action of the electromagnetic fields are used to derive the Hamiltonian part of the $d\mathbf{X}/dt$ evolution. Then the physics for the ionospheric dissipation and a loading/unloading switch on the mean pressure variable in the central plasma sheet is added. The rate of unloading of the pressure above a critical current is given by the rate of streaming along newly opened magnetic field lines (e.g. in the Near-Earth Neutral Line model [Baker et al., 1996]). The physics of the onset of parallel plasma transport for current, or equivalently current density, above a critical current is well founded in the kinetic stability analysis of tearing modes. The system is phase-space volume contracting, leading to the formation of low-dimensional attractors.

The observational justification for a global model is that the constellation of spacecraft including Geotail, Polar, Goes-8 and Goes-9 show a well correlated set of space-time signals [Pulkkinen et al., 1998], indicating a global coherence of structure that can be well modeled by a low dimensional model. Global MHD simulations also show a clear cycling of the system during substorms that suggests the large energy components are captured by low order models. The WINDMI model has been successful in representing magnetic substorms using the Bargatze et al. [1985] data [Horton and Doxas, 1998], and in giving the features of a magnetic cloud event [Horton et al., 1998]. We have chosen to use the dimensionless representation of the model [Smith et al., 1999] because the physical parameter representation has four (scaling) degrees of freedom in its fifteen parameters, which, for example, would allow us to drastically change the time-scales of the model without changing the dynamics. For the present initial study, we primarily consider the results of this model in a qualitative

sense, although the parameters were chosen with care to correspond to physical values. The parameters used for the model in the rest of this paper are given in Table 1. These parameters differ significantly from those in Horton and Dexas [1998] in only two of the fifteen physical parameters (or two of ten dimensionless parameters).

Tab. 1

If we presume our model is a fairly accurate representation of reality to the order of interest, which is global energy deposition from the solar wind input source, then it allows us to do simulations (in lieu of experiments) to resolve physical issues in the magnetosphere in a controlled manner. In Section 2 we elucidate the different types of unloading. First we consider the response of the model to constant forcing at different strengths, and will see two major types of behavior: periodic oscillations about an unstable fixed point and decay onto a stable fixed point. We postulate that these two topologically different states characterize substorms and storms, respectively. We next consider variable driving and see why it produces a chaotic response from the system. In Section 3 we look at the energy budget and energy transfer rates between the major energy components of the magnetosphere. We compare the results for storm-type driving and substorm-type driving with physical estimates. In Section 5 we give conclusions and discuss the relationship of this work to the recent review on storm-substorm relationships by Kamide et al. [1998].

2 Continuous Unloading v. Storage-unloading

The magnetosphere as described by the WINDMI model can be driven in two topologically different states, one at low forcing where there are spontaneous rapid unloading events, and one at strong forcing where the rapid unloading is always turned-on to balance the rapid loading. For the low forcing limit cycle, there are two different types of behavior depending on the variability of the forcing: for constant forcing (Section 2.1) there are periodic rapid unloading events; and for variable forcing (Section 2.2) the rapid unloading events occur with a chaotic time separation caused by the hysteresis of the system. For strong forcing the system simply decays onto a fixed point, so there is no timing to become chaotic.

2.1 Steady Driving

While strictly constant forcing is not a physically realizable situation in the magnetosphere, the ease with which the results can be interpreted make it a necessary case to consider in our analysis. Furthermore, the long periods (~ 20 hrs) of fairly steady southward IMF in the magnetic clouds may be adequately represented by constant forcing. For the model parameters used in this study, the sequence of events described here is the same for all levels of forcing below the transition to stability. The case of infrequent unloading for a low forcing state will be used as an example. Figure 2 shows the evolution of all six variables of the model at a typical constant forcing level of $V_{sw} = 0.2$. (Note that in all figures except Figures 11 and 12, the units for all axes, including time, are dimensionless.) The dynamics can be described as follows: The rate of increase of lobe current is given by the difference between the forcing and the cross-tail electric field. The pressure is also increasing such that the total time derivative of the cross-tail potential is roughly zero. This condition is equivalent to MHD pressure balance between the lobe magnetic pressure and the plasma sheet proton

Fig. 2

pressure. When the current reaches its critical value (one in the dimensionless model), a rapid unloading event occurs. The immediate effect of this is a fast drop in the pressure, shown in Figure 3. If the pressure drop is too fast, less than a few minutes, then the assumption of incompressible flow used in the derivation of the model becomes invalid. For any physically reasonable parameters satisfying the aforementioned constraints this assumption remains valid. So long as the current remains above its critical value, the pressure drops rapidly. This does not last long however, since the pressure drop (and associated current drop from $\mathbf{j} \times \mathbf{B} = \nabla P$) causes an increase in the cross-tail potential (due to Lenz's law), which in turn increases the parallel kinetic energy. Subsequently in the recovery phase, as the current drops, the potential drops and the pressure begins to rise, and finally the potential drop in the recovery phase causes both the parallel flow and perpendicular flow kinetic energy to drop, and the system returns to its initial state. This longer time scale can be followed in Figure 4. Both Figures 3 and 4 are derived from data in Figure 2. The rapid unloading event described here is also observed in the Faraday loop model of magnetospheric activity [Klimas et al., 1991] based on a dripping faucet model [Baker et al., 1990]. Where the WINDMI model differs from these is in that it provides a physical explanation of the unloading in terms of plasma sheet reconnection physics. The dynamics described above is one of the two types of unloading that occur. It consists of a loading of magnetic energy into the tail until the cross-tail current required to sustain pressure balance is large enough to trigger an instability and unload the energy. This type of unloading will be called *storage-unloading*.

Fig. 3

Fig. 4

The second type of unloading occurs for forcing (V_{sw}) strong enough that the fixed point of the lobe current is well above the critical point for the onset of rapid unloading. In this case the rapid unloading is occurring constantly. New magnetic flux is being transferred to the geotail so rapidly that the system bifurcates into a steady unloading state. Furthermore, the new system state is stable to small perturbations to this state. There are no oscillations; all variables simply decay quickly to their respective fixed points. This type of unloading will be called *continuous unloading*. We now discuss the characteristics of these states in some detail.

By taking the zero crossings of the time derivative of the ionospheric current (the minimum and maximum in an oscillation), we can obtain a bifurcation diagram with respect to forcing as shown in Figure 5. We see that there is a period-one oscillation (marked by only one minimum and one maximum position) with varying amplitude below $V_{sw} \approx 1.95$, above which there is a short interval in driving with a period doubling cascade and transition to chaos. This is followed by a stable fixed point at $V_{sw} \approx 2.0$. (This period doubling cascade to chaos is not so easy to see in the bifurcation diagram shown, but a blow-up of the region of interest does show this.) The chaotic region is relatively uninteresting for two reasons: the amplitude of oscillations are small (in physical units, ≤ 1 kV in cross-tail potential for SW driving of 100 kV); and the region of chaos is also small, making the chaos difficult to detect. (We will see more interesting chaos in section 2.2 associated with variable driving.) The system remains stable for arbitrarily strong forcing above this transition. This transition from unstable to stable dynamics is called an *inverse bifurcation*.

Fig. 5

In addition to variable amplitude oscillations shown in the bifurcation diagram, the frequency of recurrence of the rapid unloading events changes with respect to forcing as well. This is shown in Figure 6. Note that this is not a Fourier transform, but a plot of the time between unloading events for different levels of forcing. The period doubling is also more

Fig. 6

clear in this figure. For more detail we take four forcing levels and look at the ionospheric current in Figure 7. It is clear that the frequency of unloading is going up, but what is remarkable is that for weak forcing (where the recurrence time is less than the characteristic time of the system, in this case about $T = 1$) the shape of the unloading event doesn't appear to change with respect to forcing. Only the time between the events changes. Above low level forcing we see the lower edge of the oscillation lift above zero in Figure 5 as the unloading events merge into a more linear oscillation. This transition can be seen in the progression of forcing levels shown in Figure 7, culminating with the inverse bifurcation to stability at $V_{sw} = 2.1$ (not shown).

Fig. 7

2.2 Variable Driving

Here we consider the much more realistic case of variable driving, which leads to interesting behavior not attainable from constant forcing. The previous section considered only constant forcing, where the system is given time to settle onto its limit cycle and the unloading events, should there be any, occur at fixed intervals. This is a history dependent process, however, and with variable driving it is quite easy to produce a chaotic response in the magnetosphere.

We should first see what a sudden step increase in the driver does to the model. Figure 8 shows the ionospheric current for several different ten-fold increases in the forcing. For steps to strong forcing nothing interesting happens, the system simply decays to the new higher level fixed point. For steps to weak forcing however, there is an initial over-adjustment, and then relaxation to the new state. After this the system produces the periodic unloading events characteristic of the new forcing level.

Fig. 8

A decrease in forcing also introduces some new behavior to the dynamics of the system. One new feature to notice in the low forcing steps of Figure 8 is that there is a short period of inactivity after the initial step. This feature is caused by the same mechanism as the period of inactivity after a step down. Figure 9 shows the result of a single square pulse forcing function from weak forcing to strong forcing then back to weak forcing. Before the step up, the system is producing periodic unloading events characteristic of the low level of forcing. The features of interest occur between $t = 70$ and $t = 120$, after the forcing returns to its original low value. The first thing we notice is that there are no storage-unloading events – all is quiet after the storm. Examining the lobe current and pressure panels tells us why. The system must decay back to its new fixed points not at the rapid rate of strong forcing behavior, but at the much slower rate of weak forcing. Not until this is done does spontaneous rapid unloading ensue. Because of this strong dependence on the present state of the system, and therefore its history, it will be possible to see chaotic behavior for variable driving when there are a series of steps in the solar wind input.

Fig. 9

As an example of a chaotic response to variable driving, the response to a simple square wave is shown in Figure 10. The two parts of the response are particularly clear in the fifth panel for the ionospheric current loop where we also show the square wave of $V_{sw}(t)$. The first response is the directly driven part caused by the immediate redistribution of energy throughout the system in response to the higher input power. Since it is essentially a decay of the system onto a new limit cycle, it appears as a low pass filter of the square wave pulse. This is the only response to strong driving, as seen in the top panel of Figure 8. The second response to each square wave pulse in Figure 10 is the rapid unloading response discussed in

Fig. 10

Section 2.1. While these rapid unloading events will be periodic after the first, the timing from the initiation of the square pulse to the onset of the first unloading event (the spikes in I_1 and other variables) is determined by the amount of energy stored in the lobe at the start of the pulse and the new rate of input power; it is therefore history dependent. This is why there are not the same number of rapid unloading events for each pulse, even though all the pulses are the same duration.

3 Energy Budgets

In this section we compare the energy budgets and power transfer rates for the different driving levels of the system. Since this is a model based on the major energy components of the coupled magnetosphere-ionosphere system, it is of interest to follow each energy component through the evolution of the unloading. In order to facilitate the calculation of physically meaningful energies, the scales for the system shown in Table 2 were used to convert the results into physical units. The total energy of the system is given by

Tab. 2

$$E_{total} = \frac{1}{2}LI^2 + \frac{1}{2}L_iI_i^2 - MII_i + \frac{1}{2}CV^2 + \frac{1}{2}CV_i^2 + \frac{3}{2}\Omega P + K_{\parallel} \quad (1)$$

The relative contributions to the change in total energy is also interesting, and given by the derivative of Equation 1 with respect to time and using the model equations,

$$\frac{d}{dt}E_{total} = V_{sw}I - \left[\Sigma V_i^2 + \gamma I_i^{1/2} V_i^{5/2} + u_0 \Omega K_{\parallel}^{1/2} P \Theta + K_{\parallel} / \tau \right] \quad (2)$$

where the dissipation terms are all grouped in the brackets on the right. Note that in both of these equations we have used a physical representation of the model (as is necessary to obtain a meaningful form for the energy) which is equivalent to the dimensionless one described in Table 1 with the scales in Table 2.

Figure 1 is a block diagram of the energy pathways of the system, showing both the energy components and the rate of transfer between them. Transfer of energy into and out of the system, as in Equation 2, is also shown. Each (major) energy component is shown in a box, while power transfer rates are labelling their respective pathways. Larger boxes correspond to a rough grouping into magnetospheric regions; but note that the magnetic energy components cannot be uncoupled because of the mutual induction. The main energy pathway is for solar wind driving to enter through the lobes, be converted to plasma sheet convection energy, be partially converted into parallel energy and then flow out of the system. Only during unloading events is there significant transfer throughout the rest of the system.

As an example of the magnitude of the transfer rates between energy components, Figure 11 shows the magnitude of each transfer power for the event discussed in Section 2.1. These are the rates of energy transfer between the terms of Equation 1, or between the boxes in Figure 1.

Fig. 11

The two panels of Figure 12 show input power and power lost to the dissipation terms of Equation 2 on two different scales, also for the event discussed in Section 2.1. From the rate of change of the total system energy in the top panel, the rapid unloading at $t = 2.9$ is obvious, as is the more gradual unloading between $t = 3$ and $t = 4.3$. It can also be

Fig. 12

seen that the connection to the ionosphere makes no recognizable contribution to the total energy for substorm levels of forcing. (Note that the quantities plotted in lower panel are three orders of magnitude smaller than those in the upper panel.) This is not unexpected since the model assumes that only a fraction of the total plasma sheet cross-tail current is diverted into the ionosphere. Figure 12 tells us that the sudden drop in pressure causes a global rearrangement of the magnetosphere that takes a much longer time to complete. This rearrangement is characterized by an attempt by the magnetosphere to equalize the parallel flow (K_{\parallel}) and perpendicular flow ($\frac{1}{2}CV^2$) components of plasma sheet kinetic energy (MHD flow energy). However, a fraction of the energy that is converted into parallel kinetic energy is free to stream out of the system along magnetic field lines - thus unloading the confined high beta plasma.

Average values for all of the energy components and all of the power components as shown in Figure 1 are given in Tables 4 and 5 for five different levels of forcing. The difference between the two tables is that Table 4 is for constant forcing, and Table 5 is for a square wave whose maximum is the given value of forcing. For comparison, Table 3 shows the empirical energy budget of the magnetosphere for a typical storm, taken from Baker et al. [1997]. A comparison shows that the model agrees with the data reasonably well. Both show that the power input to the magnetosphere as coupled to the solar wind (IV_{sw} for the model) is on the order of 10^{11} to 10^{12} Watts. The total dissipation also corresponds well, since none of the energy is unaccounted for in the model or the empirical energy budget of Table 3 - what goes into the system must be dissipated or flow out of the system. Converting the values in the last two lines of Table 3 into power, for the assumed storm and substorm durations, we also get 10^{11} to 10^{12} Watts for total dissipation. The amount of energy dissipated in the ionosphere is the sum of lines 3 and 5 through 7 in Table 3, and is roughly 10^{10} to 10^{11} Watts. This agrees with the value of 10^9 to 10^{12} Watts for the model, given in the last two lines of Table 5, with two caveats. The lower limit in the model may more closely correspond to steady magnetospheric convection, and thus not be included in the empirical value of Table 3, and the upper limit is an overestimate to be discussed later, where we have not included important dissipation into other areas of the magnetosphere, such as the ring current.

There are several observable trend with respect to forcing in the model tables. First, there is the re-distribution of the energy flow throughout the model. As the forcing is increased, more of the energy is transferred to the ionosphere and dissipated through the nonlinear part of the ionospheric dissipation ($\gamma\sqrt{I_iV_i^5}$). This can be seen by comparing the values of the conversion between lobe field energy to plasma sheet convection energy (IV) and the equalization of flow energy ($\alpha\sqrt{PV}$) with the flow of energy from the plasma sheet to the region-1/ionosphere region (I_iV). As the forcing goes up a higher percentage of energy is dissipated in the ionosphere. For extremely high values of forcing, as in the first column of the model tables, this same trend points to a deficiency of the model and room for improvement. For $V_{sw} = 3$, the model appears to predict too much power flow into the ionosphere and dissipated there. This may be being caused by the neglect of a ring current injection mechanism in the model. As shown in Table 3, the contribution of the ring current is non-negligible. The ring current is primarily injected from the convection flow of the plasma sheet, and would therefore be a sink term extracting energy from the

Tab. 4, 5

Tab. 3

plasma sheet convection energy. This convection loss term would be expected to make a significant contribution to the dynamics for strong forcing. Since it is not present in the current model, the energy seems to be dissipated in an inappropriate place. This effect can also be seen by comparing the parallel flow out of the model (K_{\parallel}/τ) with the ionospheric dissipation ($\Sigma_1 V_i^2 + \gamma \sqrt{I_i V_i^5}$), which shows the same trend. So far as the model dynamics are concerned, the addition of a ring current should not remove the inverse bifurcation. It should change the magnitude and dynamics of the ionospheric unloading, but for very strong forcing, the rapid unloading switch will still need to be “on” in order to dissipate solar wind input energy, and the system will reside in a stable state. A second discrepancy is in the total energy stored in the tail lobes as magnetic field energy, which appears to be slightly overestimated in the model ($\frac{1}{2}LI^2$). This can most likely be explained by the simulation box for the model being larger than that assumed for the value quoted in Table 3.

With respect to the redistribution of dominant energy components with increasing V_{sw} in Table 4, we note that the mean plasma beta of the central plasma sheet, $\bar{\beta} = \bar{P}/W_B$, decreases from $\bar{\beta} = 0.1$ at low forcing where the parallel flows are relatively small, to $\bar{\beta} = 0.02$ at the strongest forcing level. Likewise, the mean Mach number for the parallel flow speed compared with the ion thermal velocity is well below one (≈ 0.1) at low forcing and just above unity at strong forcing.

4 Discussion: Storms and Substorms

Because substorms typically have spontaneous large unloading events (often not correlated with solar wind impulses) and occur for weak to medium forcing, and because storms typically are driven steadily by the solar wind and do not have identifiable spontaneous unloading events, it only makes sense to equate the two types of unloading with the two corresponding types of magnetospheric response to solar wind forcing.

Storms (continuous unloading) are the simpler of the two cases to consider. The values of the state variables, $\{I, V, P, K_{\parallel}, I_i, V_i\}$, will track their respective fixed points. When the forcing changes but remains above the stability threshold, the fixed points will move but still be stable. The system will then decay onto that new fixed point from the old at the characteristic time scale of the dynamics. This makes the overall dynamics similar to a low pass filter, as suggested by Burton et al. [1975] and Clauer et al. [1981]. When the forcing shuts off, the system will decay to its ground state through the unstable regime. But, as was discussed in Section 2.2, no more unloading events (substorms) will occur because the system will need time to recover.

Substorms (storage-unloading) are somewhat more complicated. In addition to the fixed-point-tracking ability of storms which can be interpreted as the direct driving response, the rapid unloading is of varying amplitude with respect to the base response for a given level of forcing, as shown in Figure 5, and the frequency of recurrence of the rapid unloading events changes with respect to forcing, as is shown in Figure 6. With variable driving, the timing of these rapid unloading events becomes chaotic.

We should also note that at the lowest levels of forcing, the magnitude of the oscillations is so small that it is not realistic to speak of them as substorms. Instead they should be interpreted as minor disturbances to a state of steady magnetospheric convection, possibly

as pseudo-breakups [Koskinen et al., 1993].

Even in the earliest observations of substorms, the onset of expansion was found to be an internal process of the magnetosphere which is seldom directly driven. This can be seen as the rapid unloading response of the WINDMI model which produces the large peaks in Figure 10. Another classic feature of substorms is that the most prominent auroral brightenings, which correspond to the substorm current wedge currents modeled here by the ionospheric current which produces the westward electrojet, occur during the expansion and early recovery phases of a substorm. The sharp change in the ionospheric current in Figure 10 caused by the unloading is principally from the precipitating electron contribution of the nonlinear ionospheric conductivity.

An interesting feature of the bifurcation diagram in Figure 5 is related to the fact that linear prediction filter studies [Bargatze et al., 1985] and simple bimodal models [Smith and Horton, 1998] have shown the need for increasing the direct driving component of the linear response with respect to forcing, which tells us that the true (nonlinear) response increases faster than linearly with respect to solar wind forcing. The convex shape of the bifurcation diagram (Figure 5) shows this. A linear response would produce a straight line with respect to forcing. The fact that the WINDMI response slopes upward shows that the magnitude of the response increases faster than linearly with respect to forcing - in agreement with the previous studies. This attaches a suitable physical interpretation to the need to parameterize the linear response of the magnetosphere in terms of the nonlinear response of the WINDMI model.

5 Conclusions

The shrinking of the oscillations about the fixed point with increasing strength of solar wind driving observed in the bifurcation diagram is equivalent to the view that there is an increase in the importance of the directly driven response over the less predictable storage-unloading.

We also see that the timing of the storage-unloading response is chaotic for variable forcing, which concurs with the suspected behavior of the magnetosphere [need Ref.]. This is the manifestation of the strong dependence of the evolution of the model on its present state, as well as the forcing, consistent with the history dependence of the magnetosphere.

When converted to physical units, the energy budget of this model corresponds to the inferred global values taken from measured local values [Baker, et al., 1998]. Stronger forcing causes a faster-than-linear (with respect to forcing) increase in the amount of energy unloaded into the ionosphere.

The main point of this work, however, is that there is a unified description for storms and substorms that depends only on the magnitude of the solar wind input. For weak to medium VB_s forcing we see substorms with spontaneous rapid unloading events, while for strong forcing we see only the fixed-point-tracking behavior of storms. A substorm is a manifestation of loading and unloading of stored flux in the magnetotail, and a storm is a state where the energy is continuously unloaded from the magnetotail as it is input. There is an inverse bifurcation in the energy dynamics of the magnetosphere going from weak to strong forcing.

The qualitative and quantitative descriptions given here with the WINDMI model of the

characteristics of magnetic substorms and their relationship to storms appear to provide an answer one of the questions formulated in the Kamide et al. [1998] report on the current understanding of magnetic storms, and to make inroads to the other five. (1) In regard to the solar wind sources for geomagnetic storms, a case study analysis using the energy tracking ability of the model might help answer this. (2) We cannot explicitly predict magnetic storms using the present model, but since predicting storms is a question of large-scale energy deposition, the prospect for this looks good after adding a ring current to the model. (3) The issue of storm-substorm coupling is the primary focus of this report, and we have shown how the WINDMI model gives a particular description of this coupling problem. This model would seem to be the first quantitative global model making predictions for storm-substorm relationship. (4) The model does not currently include ionospheric outflow effects, and there are no plans to add them in the immediate future; while the ionosphere may make a significant contribution to the make-up of the ring current, we believe that the primary energization (recall this is an energy-balance model) is a solar-wind-driven magnetosphere process, and is adequately described in the average quantities of this model. (5) As yet no work has been done to address the microscale process responsible for the heating of the ions to ring current energies, and given the nature of the model, it may not be possible. (6) And the final question of the validity of the Dst index is not one that can be answered by this line of investigation. The working hypothesis is that the WINDMI model provides a quantitative description of the change in behavior (bifurcation) of the magnetosphere from aperiodic substorm releases of stored energy to the storm state of continuous unloading. Clearly, this hypothesis must undergo further testing and the physical content of the model must be further expanded to make the correlations more precise and validate the model.

Acknowledgements

This work was supported by DOE grant DE-FG03-96-ER-54346 and NSF ATM 9726271.

References

- Baker, D.N., A.J. Klimas, R. L. McPherron, J. Buchner, The evolution from weak to strong geomagnetic activity: an interpretation in terms of deterministic chaos, *GRL* 17, 41 (1990).
- Baker, D.N., T.I. Pulkkinen, V. Angelopoulos, W. Baumjohann, R. L. McPherron, Neutral line model of substorms: Past results and present view, *JGR* 101, 12975 (1996).
- Baker, D.N., T.I. Pulkkinen, M. Hesse, and R. L. McPherron, A quantitative assessment of energy storage and release in the Earth's magnetotail, *JGR* 102, 7159 (1997).
- Bargatze, L. F., D. N. Baker, R. L. McPherron, E. W. Hones, Magnetospheric impulse response for many levels of geomagnetic activity, *JGR* 90, 6387 (1985).
- Blanchard, G. T. and R. L. McPherron, A bimodal representation of the response function relating the solar wind electric field to the AL index, *Adv. Space Res.* 13, 71 (1993).

- Burton, R.K., R. L. McPherron, C.T. Russel, An empirical relationship between interplanetary conditions and Dst, *JGR* 80, 4204 (1975).
- Clauer, C.R., R. L. McPherron, C. Searls, and M.G. Kivelson, Solar wind control of auroral zone geomagnetic activity, *GRL* 8, 915 (1981).
- Horton, W. and I. Doxas, A low dimensional energy conserving state space model for sub-storm dynamics, *J. Geophys. Res.* 101A, 27223 (1996).
- Horton, W., M. Pekker, and I. Doxas, Magnetic energy storage and the nightside magnetosphere-ionosphere coupling, *GRL* 25, 4083 (1998).
- Horton, W. and I. Doxas, A low dimensional dynamical model for the solar wind driven geotail-ionosphere system, *J. Geophys. Res.* 103A, 4561 (1998).
- Kamide, Y., W. Baumjohann, I.A. Daglis, W.D. Gonzalez, M. Grande, J.A. Joselyn, R.L. McPherron, J.L. Phillips, E.G.D. Reeves, G. Rostoker, A.S. Sharma, H.J. Singer, B.T. Tsurutani, V.M. Vasyliunas, Current understanding of magnetic storms: Storm-substorm relationships, *J. Geophys. Res.* 103, 17705, (1998).
- Klimas, A.J., D.N. Baker, D.A. Roberts, Linear prediction filters for linear and nonlinear geomagnetic activity, *GLR* 18, 1635 (1991).
- Klimas, A.J., D. Vassiliadis, and D.N. Baker, Data-derived analogues of the magnetospheric dynamics, *J. Geophys. Res.* 102, 26993, (1997).
- Koskinen, H. E. J., R. E. Lopez, R. J. Pellinen, T. I. Pulkkinen, D. N. Baker, T. Bösinger, Pseudobreakup and substorm growth phase in the ionosphere and magnetosphere *J. Geophys. Res.* 98, 5801, (1993).
- McPherron, R.L., D.N. Baker, L.F. Bargatze, C.R. Clauer, R.E. Holzer, IMF Control of geomagnetic activity, *Adv. Space Res.* 8, 71 (1988).
- McPherron, R.L., The Role of Substorms in the Generation of Magnetic Storms, p. 131 in “Magnetic Storms”, ed. B.T. Tsurutani, W.D. Ganzalez, Y. Kamide, J.K. Arballo, American Geophysical Union, (1997).
- Pulkkinen, T. I., D. N. Baker, L. A. Frank, J. B. Sigwarth, H. J. Opgenoorth, R. Greenwald, E. Friis-Christensen, T. Mukai, R. Nakamura, H. Singer, G. D. Reeves, M. Lester, Two sub-storm intensifications compared: Onset, expansion, and global consequences, *J. Geophys. Res.* 103, 15 (1998).
- Rostoker, G., E. Friedrich, M. Dobbs, Physics of Magnetic Storms, p.149 in “Magnetic Storms”, ed. B.T. Tsurutani, W.D. Ganzalez, Y. Kamide, J.K. Arballo, American Geophysical Union, (1997).

Smith, James P., and W. Horton, Analysis of the bimodal nature of solar wind-magnetosphere coupling, *J. Geophys. Res.* *103A*, 14917 (1998).

Smith, James P., J.-L. Thiffeault and W. Horton, Dynamical Range of the WINDMI Model: an exploration of possible magnetospheric plasma states, submitted to JGR (1999).

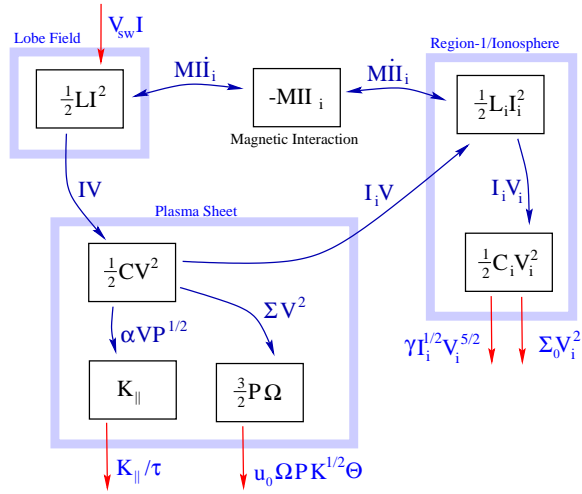


Figure 1: Block diagram for the system's energy components and power transfer rates between components.

Table 1: Model parameters

a_1	0.0467
a_2	0.00426
b_1	44.8
b_2	12.3
b_3	3.33
d_1	35000
f_1	0.156
g_1	537
g_2	4
g_3	121

Table 2: Dimensionless Scalings

S_I	3.50×10^7 A
S_V	6.52×10^4 V
S_P	7.08×10^{-11} pa
S_K	6.25×10^{14} J
S_t	1.00×10^3 s

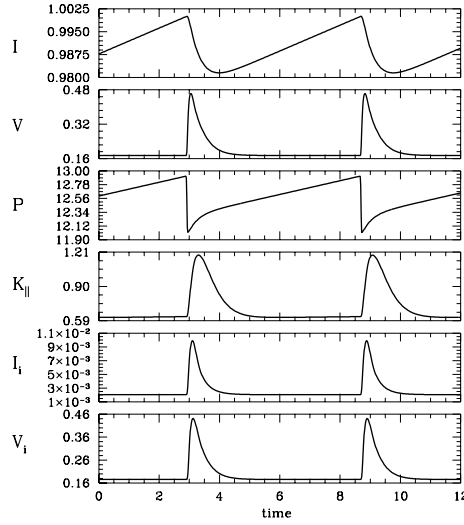


Figure 2: Substorm cycling of the WINDMI model with constant dimensionless forcing of $V_{sw} = 0.2$, typical of low level solar wind driving. Note that in all figures except Figures 11 and 12, the units for all axes, including time, are dimensionless.

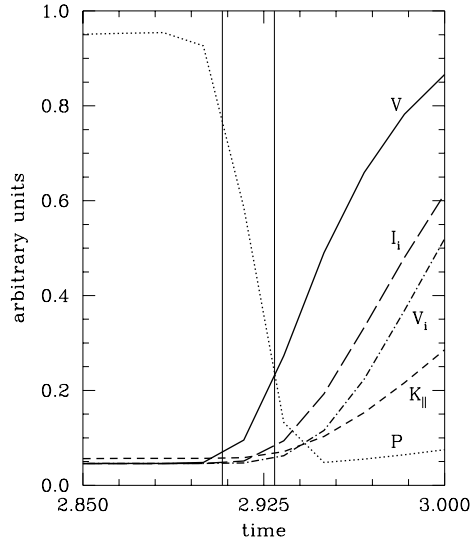


Figure 3: The rapid unloading timescale is between the two vertical lines; it is the period of time where the plasma sheet current is above the threshold.

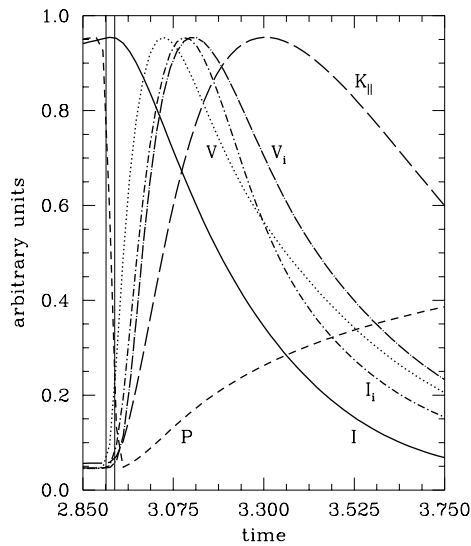


Figure 4: This is the substorm unloading timescale. The rapid unloading is still shown between the vertical lines on the left.

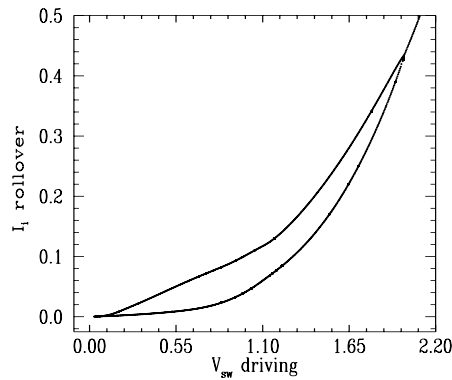


Figure 5: Bifurcation diagram with respect to forcing. Below $V_{sw} = 2.1$ the system is in a period-one oscillation (orbit connects on itself after one revolution around the unstable fixed point), In a very narrow region around $V_{sw} = 2.1$ there is period doubling and chaos, and above $V_{sw} = 2.1$ the system is stable. By showing both the minimum and maximum of an oscillation, one can see the extent of the motion about the fixed point.

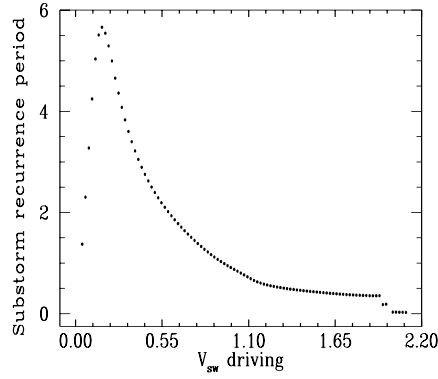


Figure 6: Substorm recurrence time with respect to forcing for constant forcing. Note from Figure 5 that the initial region having increasing period has oscillations of negligible size.

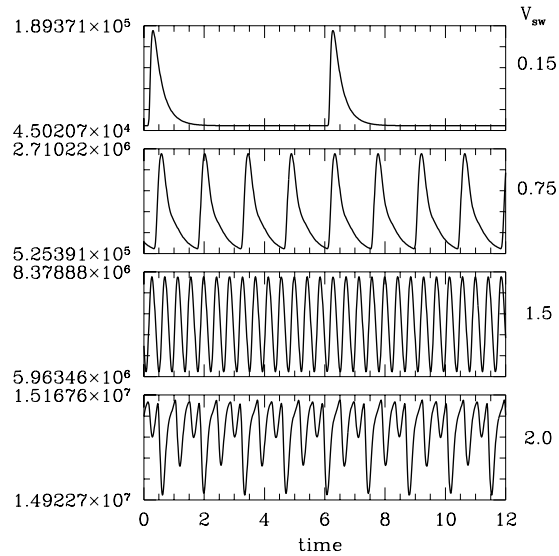


Figure 7: Ionospheric current at different levels of forcing. One can see the increasing frequency of unloading events and their eventual merging. Note that the frequency and scale of oscillations is described in Figures 5 and 6.

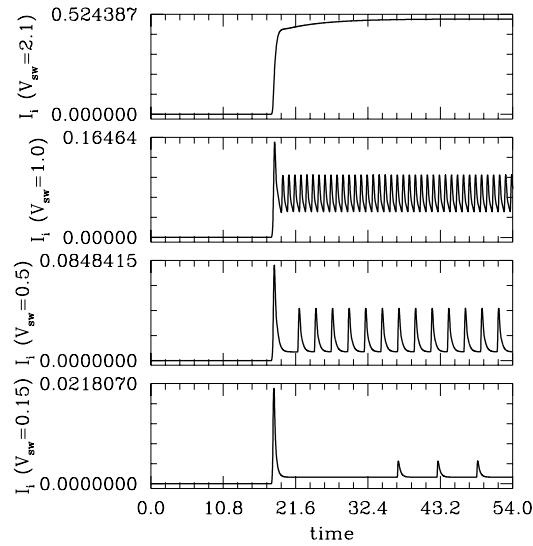


Figure 8: The effect of a sudden step-up increase in the forcing is very little. At low forcing there is an initial jump in activity followed by relaxation to the new limit cycle, otherwise the model quickly equilibrates to the new steady driving.

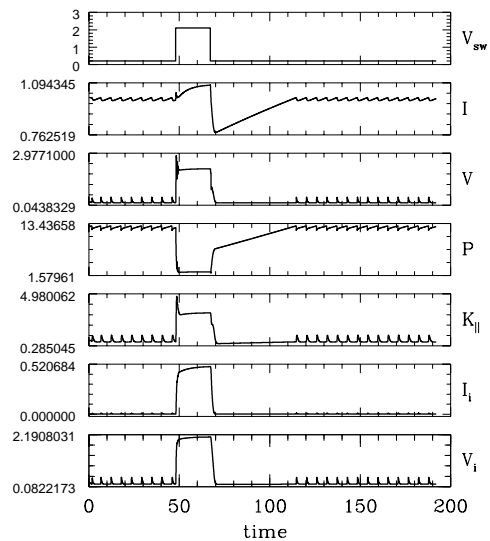


Figure 9: The six model variables for a square forcing pulse. After a strong forcing event, the current and pressure take time to recover, at the slower rate of weak forcing. The quiet after the storm can be seen in as this happens. This forcing step was from 0.2 to 2.1 and back to 0.2, and is shown in the first panel.

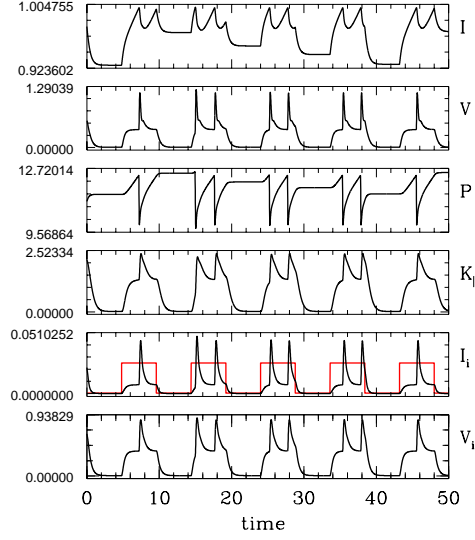


Figure 10: For a simple step function forcing, one can obtain the classic two component response of the ionosphere to the solar wind. The square-wave forcing function, V_{sw} , is shown in the fifth panel with the ionospheric current. Note that any form of variable driving introduces chaos into the timing of the rapid unloading events (onsets).

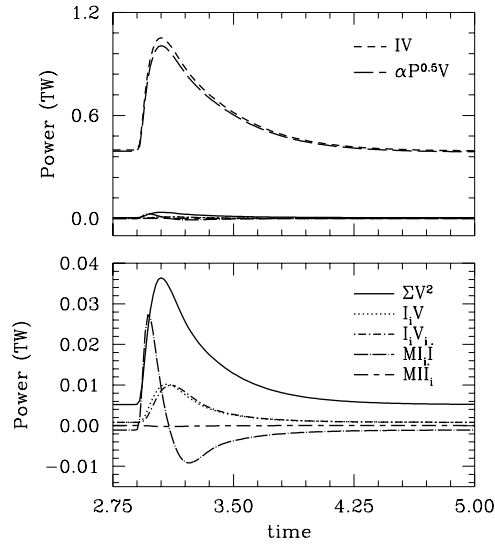


Figure 11: Power transfer rates throughout the system. One can see that only the transfer between the lobe field energy, the plasma sheet convection, and the parallel flow are nonzero during non-unloading times. This is also the primary pathway for energy flow through the system, as shown by the value of the rates during both unloading and non-unloading times.

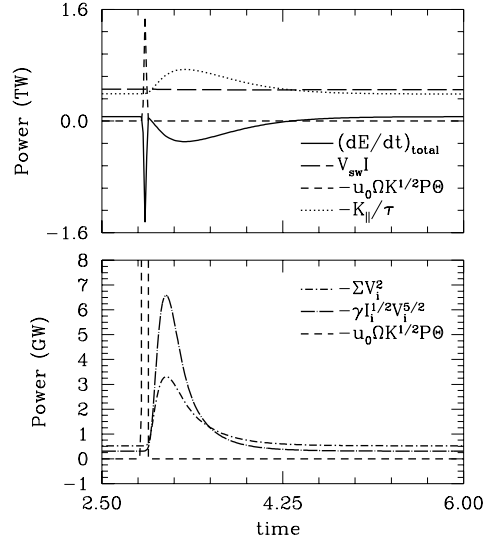


Figure 12: The different components of the total energy change. Note the two unloading timescales in the rate of change of the total system.

Table 3: Empirical Energy Budget [Baker et al., 1997].

Source and Dissipation Power (W)	
Incident solar wind	$10^{13} - 10^{14}$
SW coupled to magnetosphere	$10^{11} - 10^{12}$
Ionospheric Joule heating	$10^{10} - 10^{11}$
Ring current injection	$10^{11} - 10^{12}$
Auroral precipitation	$10^9 - 10^{10}$
Auroral luminosity	$10^8 - 10^9$
Auroral kilometric radiation	$10^7 - 10^9$
Plasmoids	$10^{11} - 10^{12}$
Energy Storage (J)	
Magnetotail	$10^{15} - 10^{16}$
Ring current	$10^{15} - 10^{16}$
Total Dissipation (J)	
Substorms (1-2 hrs)	$\sim 3 \times 10^{15}$
Major storms (>1 day)	$> 8 \times 10^{16}$

Table 4: For steady driving at fixed V_{sw}

Average energy (J)						
V_{sw}	3.0	2.1	1.5	1.0	0.5	0.2
$\frac{1}{2}LI^2$	1.1e+17	2.9e+16	2.4e+16	2.4e+16	2.4e+16	2.4e+16
MI_i^2	4.1e+15	7.3e+14	2.6e+14	8.8e+13	1.9e+13	3.5e+12
$\frac{1}{2}L_1I_i^2$	1.5e+16	1.8e+15	2.8e+14	3.6e+13	2.3e+12	7.1e+10
$\frac{1}{2}CV^2$	2.3e+14	1.1e+14	6.6e+13	2.9e+13	7.2e+12	1.1e+12
$\frac{1}{2}C_1V_i^2$	1.9e+13	9.4e+12	4.8e+12	2.2e+12	5.8e+11	9.3e+10
K_{\parallel}	3.6e+15	2e+15	2.3e+15	1.9e+15	1.1e+15	4.4e+14
$\frac{3}{2}\Omega P$	6.3e+14	4.1e+14	1.1e+15	1.6e+15	2e+15	2.1e+15
Average transfer power (W)						
V_{sw}	3.0	2.1	1.5	1.0	0.5	0.2
IV	1.5e+13	5.2e+12	3.4e+12	2.3e+12	1.1e+12	4.5e+11
$\alpha\sqrt{PV}$	3.6e+12	2e+12	2.3e+12	1.9e+12	1.1e+12	4.4e+11
ΣV^2	1.5e+12	7.5e+11	4.4e+11	1.9e+11	4.8e+10	7.5e+09
I_iV	9.7e+12	2.4e+12	6.6e+11	1.6e+11	2e+10	1.4e+09
I_iV_i	9.7e+12	2.4e+12	6.6e+11	1.6e+11	2e+10	1.4e+09
MII_i	2.3e+04	5.9e+03	-8.8e+07	-1.4e+08	-9.4e+07	-6.1e+06
$MI_i\dot{I}$	1.3e+06	4.7e+05	1.4e+08	1.7e+08	1.1e+07	1.1e+07
Average source and sink power (W)						
V_{sw}	3.0	2.1	1.5	1.0	0.5	0.2
IV_{sw}	1.5e+13	5.2e+12	3.4e+12	2.3e+12	1.1e+12	4.5e+11
$-K_{\parallel}/\tau$	-3.6e+12	-2e+12	-2.3e+12	-1.9e+12	-1.1e+12	-4.4e+11
$-u_0\Omega P\sqrt{K_{\parallel}}\Theta$	-1.5e+12	-7.5e+11	-4.4e+11	-1.9e+11	-4.7e+10	-7.2e+09
$-\Sigma_1V_i^2$	-1.5e+11	-7.5e+10	-3.8e+10	-1.7e+10	-4.6e+09	-7.4e+08
$-\gamma\sqrt{I_iV_i^5}$	-9.5e+12	-2.3e+12	-6.3e+11	-1.4e+11	-1.5e+10	-6.9e+08

Table 5: For square wave driving, $T = 69.12\tau$

Average energy (J)						
V_{sw}	3.0	2.1	1.5	1.0	0.5	0.2
$\frac{1}{2}LI^2$	3.4e+16	2e+16	2.1e+16	2.2e+16	2.3e+16	2.4e+16
MI_i^2	8.4e+14	2.9e+14	1.2e+14	4.2e+13	9.3e+12	1.8e+12
$\frac{1}{2}L_1I_i^2$	2.5e+15	6.6e+14	1.2e+14	1.6e+13	1.1e+12	3.6e+10
$\frac{1}{2}CV^2$	9e+13	5.2e+13	3.1e+13	1.4e+13	3.5e+12	5.5e+11
$\frac{1}{2}C_1V_i^2$	7.3e+12	4.2e+12	2.2e+12	1e+12	2.8e+11	4.6e+10
K_{\parallel}	1.7e+15	1.1e+15	1.2e+15	9.7e+14	5.3e+14	2.2e+14
$\frac{3}{2}\Omega P$	7.8e+14	8.5e+14	1.3e+15	1.7e+15	2e+15	2.1e+15
Average transfer power (W)						
V_{sw}	3.0	2.1	1.5	1.0	0.5	0.2
IV	4.7e+12	2.4e+12	1.7e+12	1.1e+12	5.7e+11	2.3e+11
$\alpha\sqrt{PV}$	1.7e+12	1.1e+12	1.2e+12	9.7e+11	5.4e+11	2.2e+11
ΣV^2	6e+11	3.5e+11	2.1e+11	9.1e+10	2.3e+10	3.7e+09
I_iV	2.4e+12	9.4e+11	2.9e+11	7.3e+10	9.6e+09	7.1e+08
I_iV_i	2.4e+12	9.4e+11	2.9e+11	7.3e+10	9.6e+09	7.1e+08
MII_i	-2.4e+09	-9.2e+08	-2.8e+08	-1.1e+08	-5.2e+07	-3.5e+06
$MI_i\dot{I}$	2.3e+09	8.9e+08	2.4e+08	2.5e+08	8.5e+07	2.9e+06
Average source and sink power (W)						
V_{sw}	3.0	2.1	1.5	1.0	0.5	0.2
IV_{sw}	4.7e+12	2.4e+12	1.7e+12	1.1e+12	5.6e+11	2.3e+11
$-K_{\parallel}/\tau$	-1.7e+12	-1.1e+12	-1.2e+12	-9.7e+11	-5.3e+11	-2.2e+11
$-u_0\Omega P\sqrt{K_{\parallel}}\Theta$	-6e+11	-3.5e+11	-2.1e+11	-9.2e+10	-2.4e+10	-3.6e+09
$-\Sigma_1V_i^2$	-5.9e+10	-3.4e+10	-1.8e+10	-8.2e+09	-2.2e+09	-3.6e+08
$-\gamma\sqrt{I_iV_i^5}$	-2.3e+12	-9.1e+11	-2.8e+11	-6.5e+10	-7.3e+09	-3.5e+08